Electron Precipitation Curtains - Simulating the Microburst Origin Hypothesis

Thomas Paul O'Brien[1], Colby Lemon[1], and J Bernard Blake[1]

[1]The Aerospace Corporation

November 24, 2022

Abstract

We explore the hypothesis that electron precipitation curtains such as those observed by the AeroCube-6 satellite pair can be produced by electron microbursts. Precipitation curtains are latitudinal structures of stable precipitation that persist for timescales of 10s of seconds or longer. The electrons involved have energies of 10s-100s of keV. The microburst formation hypothesis states that a source region in the equatorial region produces a series of very low frequency chorus wave emissions. Each of these emissions in turn produces a microburst of electron precipitation, filling the drift and bounce loss cone on the local field line. Electrons in the drift loss cone remain on the field line and bounce-phase mix over subsequent bounces while also drifting in azimuth. When observed at downstream azimuths by a satellite equipped with an integral energy sensor, no bounce phase structure remains, or, equivalently, the same time profile is present when two such satellites pass by many seconds apart. The spatial structure that remains reflects the pattern of microburst sources. Statistical studies of where and when curtains occur have indicated that some, but not all, curtains could be caused by microbursts. We use test particle tracing in a dipole magnetic field to show that spatially stationary source regions generating periodic microbursts can produce curtain signatures azimuthally downstream. We conclude that one viable explanation for many of the curtains observed by the AeroCube-6 pair is the accumulation of drift-dispersed microburst electron byproducts in the drift loss cone.

Electron Precipitation Curtains – Simulating the Microburst Origin Hypothesis

For submission to JGR Space Physics

T.P. O'Brien, C.L. Lemon, and J.B. Blake

Space Science Applications Lab, The Aerospace Corporation, El Segundo, California, USA.

Corresponding Author: T. Paul O'Brien
14301 Sullyfield Circle, Unit C, CH1-515
Chantilly, VA, 20151
paul.obrien@aero.org

Running Title: MICROBURST-CURTAIN SIMULATION

Key Points:

- Curtains are small-scale latitude structures observed by a pair of low altitude satellites
- We use test particle tracing to investigate the origin of curtains
- Curtains can be caused by microbursts, which are transient, smaller-scale structures

Abstract

We explore the hypothesis that electron precipitation curtains such as those observed by the AeroCube-6 satellite pair can be produced by electron microbursts. Precipitation curtains are latitudinal structures of stable precipitation that persist for timescales of 10s of seconds or longer. The electrons involved have energies of 10s-100s of keV. The microburst formation hypothesis states that a source region in the equatorial region produces a series of very low frequency chorus wave emissions. Each of these emissions in turn produces a microburst of electron precipitation, filling the drift and bounce loss cone on the local field line. Electrons in the drift loss cone remain on the field line and bounce-phase mix over subsequent bounces while also drifting in azimuth. When observed at downstream azimuths by a satellite equipped with an integral energy sensor, no bounce phase structure remains, or, equivalently, the same time profile is present when two such satellites pass by many seconds apart. The spatial structure that remains reflects the pattern of microburst sources. Statistical studies of where and when curtains occur have indicated that some, but not all, curtains could be caused by microbursts. We use test particle tracing in a dipole magnetic field to show that spatially stationary source regions generating periodic microbursts can produce curtain signatures azimuthally downstream. We conclude that one viable explanation for many of the curtains observed by the AeroCube-6 pair is the accumulation of drift-dispersed microburst electron byproducts in the drift loss cone.

Plain Language Summary

The pair of low altitude, polar AeroCube-6 satellites observed stable small-scale structure in the electrons present in low Earth orbit (LEO). Even when the two vehicles are separated in time by over a minute, both measure roughly the same structured time profile of radiation intensity, offset by the time separation between vehicles. Individual features in this stable structure are known as curtains. We test whether the curtains could be formed by accumulation of electrons from short-lived microbursts of radiation intensity, which individually last less than a second. Accordingly, each microburst adds electrons to the population that reaches LEO but does not enter the atmosphere before drifting into the atmosphere in the South Atlantic Anomaly. Because microbursts contain many energies, over time the sub-second temporal structure will spread out during the bounce and drift motion of the electrons. Further, if the microburst source repeatedly produces bursts in the same location, fluxes from new and old bursts will eventually overlap. Thus, it is possible that satellites in LEO with wide-energy sensors to see a stable temporal profile reflective of the spatial structure of the microburst source locations. We demonstrate this hypothesized mechanism by tracing electrons in a dipole magnetic field.

Keywords

Radiation belts, particle precipitation, electron microbursts, chorus

1 Introduction

In *Blake and O'Brien* (2016), we described the observation of persistent fine-scale (~tens km, >60 sec duration) electron precipitation structures observed in low Earth orbit. Because atmospheric losses play a major role in determining the state of the radiation belts, we wish to test this hypothesis to understand better the underlying loss mechanisms. The curtain observations were made using the AeroCube-6 (AC6) pair of CubeSats. We hypothesized that the stable fine-scale structures were produced by accumulation of microburst fluxes in the drift loss cone which, after many drifts, had bounce-phase mixed to the point that the flux appears steady in a sensor with an integral or broadband response. AC6 carries dosimeters that have quasi-integral energy response, and the curtains were observed in the DOS1 low energy dosimeter. In this paper, we investigate this hypothesis using test particle tracing. We note that *Shumko et al.* (2020a) introduced an additional hypothesis involving parallel electric fields lowering the mirror point altitude, but we will not test that hypothesis here.

The top of Figure 1 depicts how microbursts from a near and far sources place particles in the drift and bounce loss cones. The drift loss cone (DLC) consists of particles that are destined to enter the atmosphere upon drifting into the South Atlantic Anomaly. The existence of the DLC arises because of the offset of the Earth's dipole magnetic field from its center of mass. The bounce loss cone (BLC) consists of particles that will enter the atmosphere before completing a full bounce motion. (In the Earth's field, the northern and southern bounce loss cones are not the same size due to the dipole offset.) Only particles in the drift loss cone can be seen from the drift-conjugate source far from the observing satellite, whereas the sensor can observe particles from bounce-conjugate near source in both the drift and bounce loss cones. For particles from the near source, all energies arrive nearly simultaneously at the sensor producing temporal features on timescales shorter than the bounce period (<~1 second). For particles from the far source, over the course of multiple bounces between the source and the sensor, the particles bounce phase mix, stretching out the initial packet in time and space. If enough time passes between the source and the sensor, a sensor that integrates over a broad energy range will not be able to distinguish the remaining energy-time structure in the stretched-out packet. As packets are drawn out to greater and greater extent, the sensor will see a continuous count rate on the drift shell connecting it to the far source region. In this manner, the count rate observed at the sensing spacecraft represents the intensity and distribution in drift shell (latitude or L shell) of far sources in the form of curtains, with possible microbursts from near sources superimposed.

The bottom of Figure 1 takes a larger view, showing how the drifting particles eventually enter the atmosphere at the South Atlantic Anomaly (SAA). It is noteworthy that a Satellite in the northern hemisphere on field lines conjugate to the SAA will see only particles scattered on the local field lines – it is entirely in the bounce loss cone. When curtains are observed in this location, the microburst origin hypothesis cannot apply because there is no time for particles to bounce phase mix before being measured by the satellite. *Shumko et al.* (2020a) did observe some such cases, meaning that the hypothesis under study here cannot be the only true explanation for curtains.

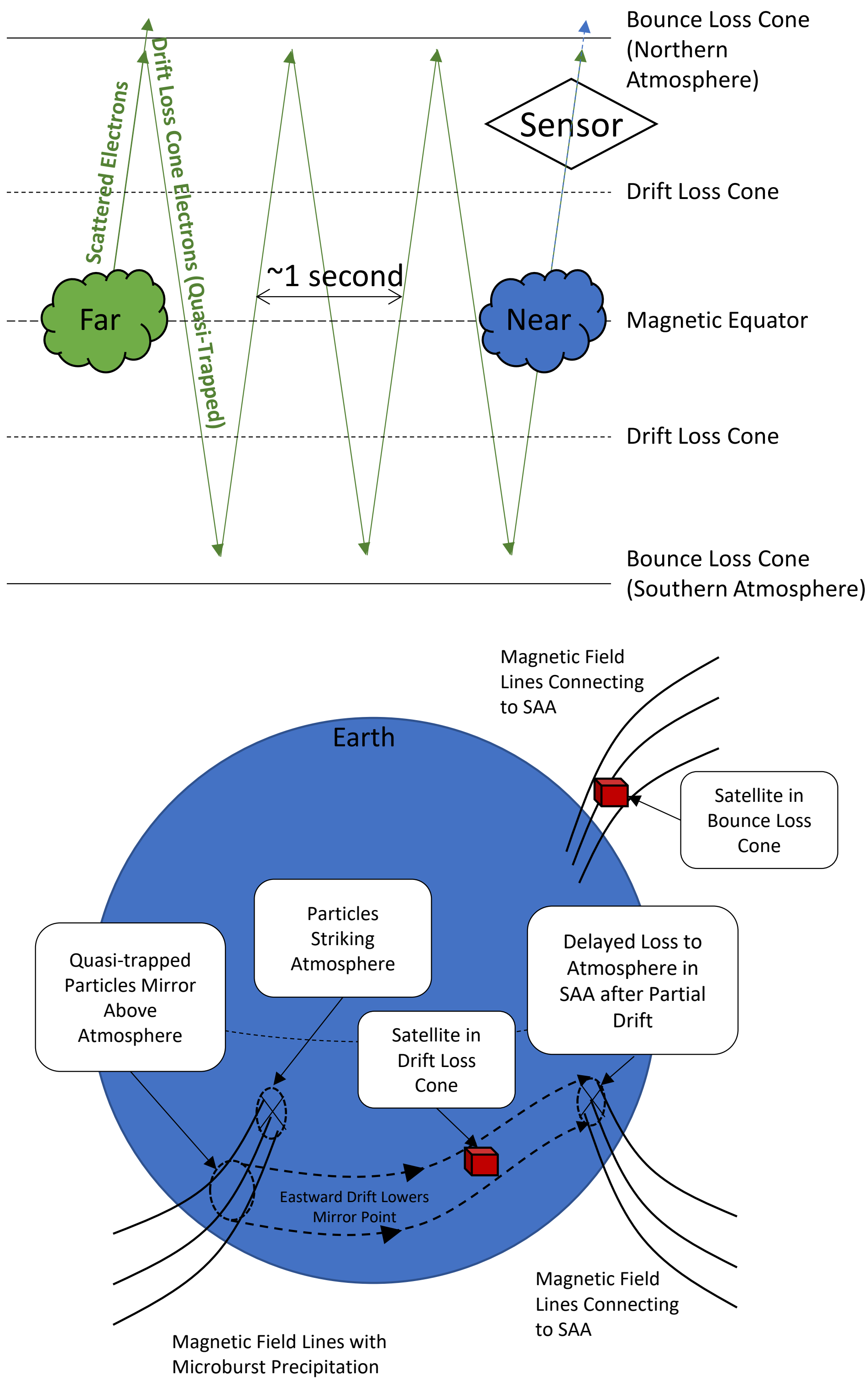

Figure 1. Top: Schematic of microburst formation by a near source and curtain formation by a far source. Bottom: Schematic of quasi-trapped particles in the drift loss cone until they strike the atmosphere in the South Atlantic Anomaly (SAA).

For our numerical experiment, we need to know the size and spectrum of microbursts, as well as their temporal properties: “on” time and pulse repeat period. We have in situ observations to support estimates of most of these parameters. However, in some cases, we will need to rely on properties of chorus waves and their source region to provide additional constraints, relying on the well-supported connection between chorus and microbursts (e.g., *Lorentzen et al.*, 2001a; *Breneman et al.*, 2017; *Kawamura et al.*, 2021). For the size of the microburst source regions, we rely on *Shumko et al.* (2020b) who found that most microbursts had a diameter less than 200 km (radius < 100 km) when projected to the magnetic equatorial plane, but some were quite a bit larger. A radius less than 100 km is consistent with the phase coherence scale of chorus and small-scale plasma irregularities (*Santolik et al.*, 2004; *Agapitov et al.*, 2011;2017;2018;2021 *Hosseini et al*., 2021). Because the curtains are hypothesized to superimpose many microbursts, a larger spatial scale is also relevant: the amplitude coherence scale length of chorus in the equatorial plane. This scale has most recently been estimated to be ~300 km in radius (*Agapitov et al.*, 2017; 2018; 2021), with larger values possible for lower chorus amplitudes. We will vary the size of the equatorial source region to replicate observed count rates at AC6. However, when performing parametric surveys, we will adopt a reference radius of 75 km, following *Shumko et al.* (2020b).

For the spectrum of microbursts, there are two main estimates, an exponential spectrum with an e-folding of 20-40 keV depending on activity level form *Lee et al.* (2005), and a more recent estimate 40-150 keV from *Johnson et al.* (2021). We adopt 70 keV, the mode from *Johnson et al.*

Borrowing from the chorus hypothesis, we estimate the temporal “on” time of the microbursts to be about 0.1 s, based on the time duration of a chorus riser (e.g., *Santolik et al.*, 2004; *Nishimura et al.* 2010; 2011 and references therein). The repeat time for microbursts is also taken from chorus, and is adopted as 0.7 s, after *Shue et al.* (2015).

In the remainder of this paper, we will examine the in-situ particle data used, then describe the test particle tracing, next we will use the simulation to examine idealized and real cases. Finally, we will discuss our results, which show that microbursts can produce curtains, consistent with the hypothesis from *Blake and O’Brien*.

2 Data

The primary data we use for this mission is the DOS1 sensor from AeroCube-6 (*O’Brien et al.*, 2016). The AC6 pair, designated AC6-A and AC6-B, was launched 19 June 2014 and regularly collected data through 2017. The orbit is approximately 620 × 700 km with an 98° inclination. The spacecraft separation varied over the course of the mission, but in the case studied here, the AC6-B spacecraft was about 65 seconds behind the AC6-A spacecraft. Each spacecraft carries three dosimeters. DOS1 is a dosimeter with an electronic threshold of 30 keV for a particle to register, and 263.5 μRads per count

(*O'Brien et al.*, 2016). Figure 2 shows the DOS1 response (*O'Brien et al.,* 2019) to electrons along with weighted responses for exponential spectra. The other two dosimeters on each satellite are not used in this study. While the dosimeters record data at 1 Hz and 10 Hz, 10 Hz data are intermittent and not used here.

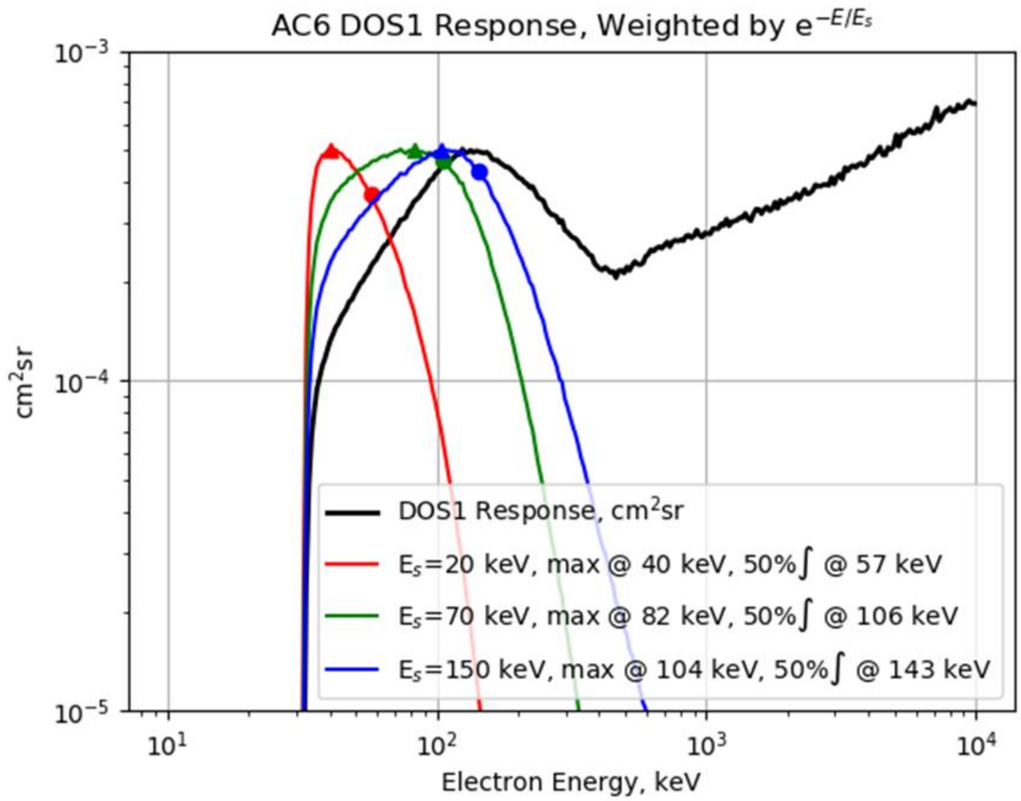

Figure 2. DOS1 response to isotropic electrons. The black trace is the response itself, while the colored traces (arbitrary units) indicate the response weighted by an exponential spectrum. Triangles indicate the peak of each weighted response, while circles indicate the midpoint energy, below which 50% of the counts originate for such an exponential spectrum. For steeper spectra (smaller E_s) the response is dominated by electrons closer to the ~30 keV threshold response.

Supporting data for this study come from NASA's Van Allen Probes. The probes were in a near-equatorial elliptical orbit with low altitude perigee and apogee slightly inside geostationary orbit. We use the merged electron spectrum product from the Radiation Belt Storm Probes (RBSP) Energetic Particle Composition and Thermal Plasma (ECT) suite (*Boyd et al.*, 2019). We also use plasmapause locations identified by the wave suite, Electric and Magnetic Field Instrument Suite and Integrated Science (EMFISIS) (*Kletzing et al.*,2013).

The merged RBSP ECT product provides spline fits to selected, cleaned, spin-averaged flux channels from ~15 eV to 20 MeV. We convolve the splines with the DOS1 energy response to estimate what a DOS1 sensor would see at the equatorial orbit of Van Allen Probes at the same L shells as AC6.

3 Dipole Particle Tracing Simulation

We implement a test particle simulation in a dipole magnetic field with no electric field. Each test particle (electron) is traced backwards in time from its encounter with AC6, accumulating source contributions until it strikes the atmosphere or leaves the azimuth range of the sources. In a pure dipole there is no drift-loss cone, only a bounce loss cone. However, we can emulate a drift loss cone by limiting the azimuth range of the simulation. We first assume that sufficiently far backward in azimuth there is an unstructured source of "background" flux. To each scene simulated, we add equatorial sources that contribute phase-space density (PSD) to particle trajectories that pass northbound through the equator. The sources we use will be pulsed in time.

To trace a particle, first we determine whether it is in the bounce loss cone. All particles with a dipole mirror point below $h_{lc} = 100$ km are considered in the BLC. For such particles, we determine whether they are heading northward away from the equator on their first half-bounce. If so, then the equatorial crossing is found and any sources at that location contribute to the particle's PSD. Otherwise, the particle carries zero flux, as it will be lost to the atmosphere before encountering a source during the backtrace. For particles that are not in the BLC, they are assumed to be in the DLC, and the tracing code finds each northward equatorial crossing and adds PSD from any sources at those crossings. DLC particles are traced backward until they leave the azimuth range where sources have been placed.

The following mathematical treatment is synthesized from *Northrop and Teller* (1960), *Schulz and Lanzerotti* (1974), section I.4, *Walt* (1994) chapter 2, and *Orlova and Shprits* (2011). The simulation uses dipole coordinates: field line label L, magnetic colatitude θ, and longitude φ. In some cases, we will use magnetic latitude $\lambda = \frac{\pi}{2} - \theta$ in place of colatitude. The magnetic field is given by:

$$\vec{B}(L,\theta,\varphi) = -\frac{B_0}{L^3}\frac{\left(2\hat{r}\cos\theta + \hat{\theta}\sin\theta\right)}{\sin^6\theta}$$

Here $B_0 = 31{,}000$ nT is the adopted value of the equatorial field strength at the surface of the Earth, and $\hat{r}$ and $\hat{\theta}$ are the radial and colatitude unit vectors (there is no azimuthal component for a dipole field, which would have unit vector $\hat{\varphi}$). The guiding center longitudinal drift in a dipole field is given by:

$$\vec{u}_d = \frac{m_0\gamma}{qB^3}\left(\frac{{v_\perp}^2}{2} + {v_\parallel}^2\right)\vec{B}\times\vec{\nabla}B = \frac{d\varphi}{dt}\hat{\varphi}$$

Here $\gamma = 1/\sqrt{1-(v/c)^2}$ is the relativistic factor for velocity v and speed of light c, q is the signed electron charge, B is the local magnetic field magnitude, m_0 is the rest mass, $v_\perp = v\sin\alpha$ is the perpendicular velocity, and $v_\parallel = v\cos\alpha$ is the parallel velocity, and α is the particle's local pitch angle.

The bounce motion is given by:

$$\frac{d\theta}{dt} = \frac{v_\parallel}{\left(\frac{ds}{d\theta}\right)_L} = -\frac{v_\parallel}{LR_E(1+3\cos^2\theta)^{\frac{1}{2}}\sin\theta} = -\frac{d\lambda}{dt}$$

where $R_E = 6371$ km is the adopted radius of the Earth.

First, we compute the mirror magnetic field strength

$$B_m = \frac{B(L,\theta,\varphi)}{\sin^2\alpha}$$

Next, we compute the equatorial pitch angle α_{eq}:

$$\sin^2\alpha_{eq} = \frac{B(L,\pi/2,\varphi)}{B_m}$$

Then we compute the mirror latitude, λ_m by solving:

$$\sin^2\alpha_{eq} = \frac{\cos^6\lambda_m}{\sqrt{1+3\sin^2\lambda_m}}$$

To determine whether the particle is in the BLC or DLC, we need to know the loss cone latitude λ_{lc}, which is given by:

$$\cos^2\lambda_{lc} = \frac{R_E + h_{lc}}{LR_E}$$

This equation arises from the radius of the particle: $r = LR_E\sin^2\theta = LR_E\cos^2\lambda$. A particle is in the BLC if $\lambda_m > \lambda_{lc}$, and in the DLC otherwise. A BLC particle can only reach the spacecraft from an equatorial northward source region if it reaches the spacecraft in the northern hemisphere ($\lambda \geq 0$) with an acute local pitch angle ($\alpha < \pi/2$), otherwise it would strike the atmosphere between its source region and reaching the spacecraft.

Whether a particle is in the DLC or BLC, the next thing we need to know is when and where it last crossed the equator passing northward. The travel time between the equator and a latitude λ for a particle with mirror latitude λ_m is given by:

$$T(\lambda;\lambda_m,L,v) = \int_0^\lambda \frac{dt}{d\lambda/dt} = \frac{LR_E}{v}V(\lambda;\lambda_m)$$

where $V(\lambda;\lambda_m)$ is:

$$V(\lambda;\lambda_m) = \int_0^\lambda \frac{\cos\lambda\,(1+3\sin^2\lambda\,)^{\frac{1}{2}}}{\left(1-\frac{(1+3\sin^2\lambda\,)^{\frac{1}{2}}}{C(\lambda_m)\cos^6\lambda}\right)^{1/2}}d\lambda$$

$$C(\lambda_m) = \frac{(1+3\sin^2\lambda_m\,)^{\frac{1}{2}}}{\cos^6\lambda_m} = \frac{1}{\sin^2\alpha_{eq}}$$

The particle's bounce period is then

$$\tau_b = 4T(\lambda_m;\lambda_m,L,v)$$

During the travel from the equator to a latitude of λ, a particle drifts in azimuth

$$\Delta\varphi(\lambda;\lambda_m,L,v) = \int_0^\lambda \frac{d\varphi/dt}{d\lambda/dt}d\lambda = \frac{M}{LR_E\gamma qv}W(\lambda;\lambda_m)$$

M is the first adiabatic invariant:

$$M = \frac{p^2}{2m_0 B_m}$$

with $p = m_0 \gamma v$ being the momentum, and $W(\lambda; \lambda_m)$ is:

$$W(\lambda; \lambda_m) = \int_0^\lambda \frac{3(1+\sin^2\lambda)}{\cos^3\lambda\,(1+3\sin^2\lambda\,)} \frac{\left(1 - 2\frac{B_m}{B(\lambda)}\right)}{(1 - B(\lambda)/B_m)^{1/2}} d\lambda$$

$$\frac{B(\lambda)}{B_m} = \frac{(1+3\sin^2\lambda\,)^{\frac{1}{2}}}{C(\lambda_m)\cos^6\lambda}$$

Northbound particles take time $T(\lambda; \lambda_m, L, v)$ to reach the spacecraft at λ in the northern hemisphere, while southbound particles take an addition $3T(\lambda_m; \lambda_m, L, v)$. Likewise, northbound particles travel $\Delta\varphi(\lambda; \lambda_m, L, v)$ to reach the spacecraft, while southbound particles take an additional $3\Delta\varphi(\lambda_m; \lambda_m, L, v)$. Over a complete bounce period, the particle drifts:

$$\Delta\varphi_d = 4\Delta\varphi(\lambda_m; \lambda_m, L, v)$$

We can use these equations for equations for T and $\Delta\varphi$, τ_b, and $\Delta\varphi_d$ to compute the time and location of the most recent northward equatorial crossing given an initial latitude and pitch angle. Then each prior northward equatorial crossing is one bounce period earlier and is displaced in longitude by $-\Delta\varphi_d$. At each northbound equatorial crossing, we add PSD to the test particle for any sources that overlap its equatorial crossing. We note that because the particles do not change momentum over the course of their motion, we can accumulate unidirectional differential flux (j) rather than PSD ($f = j/p^2$).

Our source regions are isotropic and circles in the equatorial plane, and it is helpful, then to be able to compute the distance between the particle's equatorial crossing $(L, \pi/2, \varphi)$ and the source region's center $(L_s, \pi/2, \varphi_s)$. We perform this distance calculation in cartesian coordinates using the general transform:

$$x = r\sin\theta\cos\varphi$$
$$y = r\sin\theta\sin\varphi$$
$$z = r\cos\theta$$

When relating this system to AC6 data, θ and φ are taken to be geographic coordinates, since the dipole tilt is small, and all longitudes are relative in the simulation.

Altogether, this mathematical framework allows us to place sources at the equator and sum up their contributions to particles reaching the AC6 location. We do this for particles with energies spanning E_1 to E_2, and for local pitch angles 5° to 175°. The energy limits E_1 and E_2 are chosen such that the sensor response weighted by the exponential spectrum is at least a factor of 100 of its peak value; this ensures that the integral captures >99% of count rate without including unneeded energies and slowing down some of the calculations. For an exponential spectrum with characteristic energy of 70 keV, these energy integral limits are ~30 keV to ~300 keV. Similarly, we exclude pitch angles within 5° ($\frac{\pi}{36}$ radians) of the field-line to avoid computational singularities for field-aligned particles; at AC6, such particles are deep within the loss cone and constitute a very small solid angle.

Each particle arrives at AC6 with an accumulated unidirectional different flux. We convert that to omnidirectional flux (J) using:

$$J(E) = 2\pi \int_{\pi/36}^{\frac{\pi}{2}-\frac{\pi}{36}} j(E, \alpha) \sin \alpha \, d\alpha$$

We convolve that with the energy response $R_{\mathrm{DOS1}}(E)$ of the DOS1 sensor on AC6. The count rate in DOS1 is:

$$c_{\mathrm{DOS1}} = \int_{E_1}^{E_2} J(E) R_{\mathrm{DOS1}}(E) dE$$

We perform this calculation for every time point along the AC6 trajectory.

4 Simulation Results

Each of our simulations involves placing one or more microburst sources in the equatorial plane, and then flying AC6-A and AC6-B through that scene. For initial test cases, we will use circular sources with a given center (L_s,φ_s) and radius (r_s). Each source has a source size (r_s), energy scale (E_s), pulse period (T_s) and pulse width (ΔT_s), and an isotropic differential flux spectrum $j_s e^{-E/E_s}$. These sources will have constant flux within their spatial extent, and all start their first pulse at zero seconds into the simulation. For the real scene, we will use a Gaussian source described below, with pulse phase randomized for each source.

4.1 Simulations of idealized sources

We perform a set of idealized simulations to determine how different parameters of the source regions affect the dosimeter count rate at AC6. In each such simulation the AC6 vehicles fly along φ=0 longitude, and sources are place at negative longitudes so that their electrons will drift toward the AC6 trajectory. To understand source placement and its consequences, we need to examine the drift and bounce periods for electrons that stimulate DOS1 on AC6. Figure 3 shows that for an e^{-E/E_s} spectrum with $E_s = 70$ keV, the particles that drive the DOS1 response have energies ~30-300 keV. At $L = 5$ and $\alpha_{eq} = 45°$, the ratio of bounces per degree of drift for such particles is in the ranges from ~48 at low energy to ~14 at higher energy. The bounce period runs from just over a second down to half a second, while the drift time ranges from ~55 down to ~7 seconds per degree. For a source with a radius $r_s = 75$ km at the equator at $L_s = 5$, the vehicle takes about a second to traverse the source, and the source has a longitudinal extent (across the diameter) of about 0.25°.

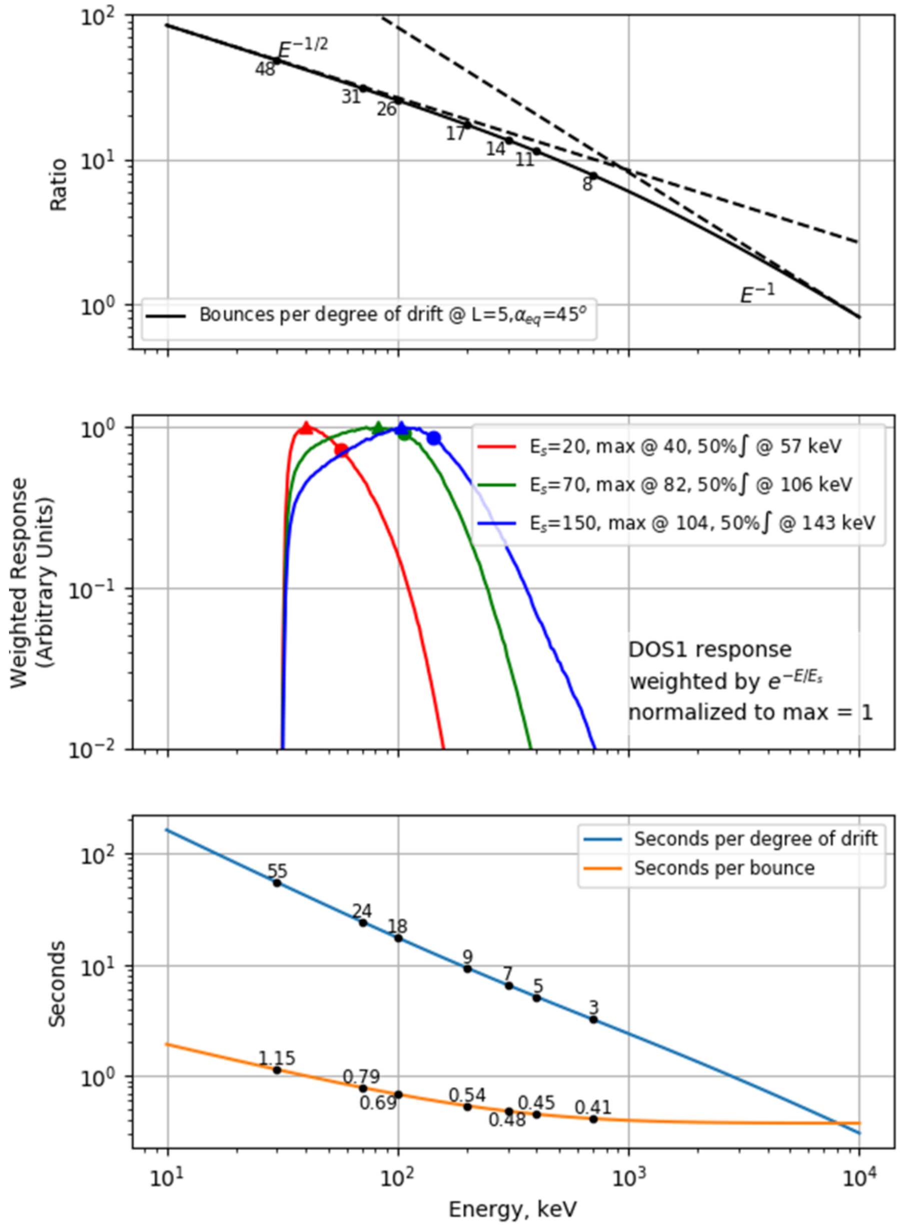

Figure 3. Drift and bounce periods for electrons counted by DOS1. Top: the number of bounces per degree of drift. Middle: the normalized, weighted DOS1 response, with peak and 50th percentile responses marked. Bottom: Bounce and drift periods. All calculations are performed at $L = 5$, $\alpha_{eq} = 45°$.

For our first experiment, we will place sources 0°, 0.1°, 0.2°, 0.5°, and 1° west of the AC6 trajectory. AC6-B trails AC6-A by 59.75 seconds, at $L = 5$.

In Figure 4 we see the results of running this simulation with 100 local pitch angles and 50 Hz time sample, averaged to 1-second averages. The nearest sources are bounce conjugate to the AC6 trajectory, and they produce spikes from bounce loss cone flux contributing to the DOS1 rate. We also see that a gradual increase in the level of the non-spike DOS1 rate from the 0 to 0.2° sources. As with microbursts, the spikes are at different times (locations) for the two satellites (i.e., at different times even after AC6-B is shifted by a time corresponding to its trailing distance). The non-spike portion is the same at both spacecraft, as observed for curtains. The far sources at 0.2° or more west of the source are only drift conjugate to the AC6 trajectory, and they produce curtain-like steady-state DOS1 rate at AC6. The steady state rate c_{ss} (formulated below) also resembles the circular shape of the source region, as the flux reaching AC6 is proportional to the path length of the drift trajectory through the source region. Neglecting the slight curvature of the drift path through the source region ($r_s \ll L_s R_E$), the path length through the region is:

$$\Delta\ell \approx 2\sqrt{r_s^2 - (L - L_s)^2 R_E^2}, |L - L_s| < \frac{r_s}{R_E}$$

For a Gaussian source that extends to $3r_s$, having an intensity dependence $e^{-\frac{1}{2}(d/r_s)^2}$, where d is the distance from the source's center, the equivalent path length is:

$$\Delta\ell \approx \sqrt{2\pi} r_s e^{-\frac{1}{2}\frac{(L-L_s)^2 R_E^2}{r_s^2}} \operatorname{erf}\left(\sqrt{\frac{9}{2} - \frac{1}{2}\frac{(L-L_s)^2 R_E^2}{r_s^2}}\right), |L - L_s| < \frac{3r_s}{R_E}$$

where $\operatorname{erf}(z) = \frac{2}{\sqrt{\pi}}\int_0^z e^{-t^2} dt$ is the Gauss error function.

At $L = 5$, in the time it takes to travel 0.2°, particles driving the DOS1 response under an $E_s = 70$ keV spectrum will have been drifting for ~1-11 seconds and have bounced ~2-10 times. That is a significant amount of bounce dispersion, and even slightly more occurs in the time to drift from one side of the source region to the other. The pulsing of the source supplies new flux for 0.1 seconds repeating every 0.7 seconds, which is about every bounce period. The pulsing sustains and further smooths out the fluxes downstream of the source region. Non-repeating sources would also contribute flux, but their flux would presumably decrease with distance from the source as drift dispersion stretches out the initial source flux.

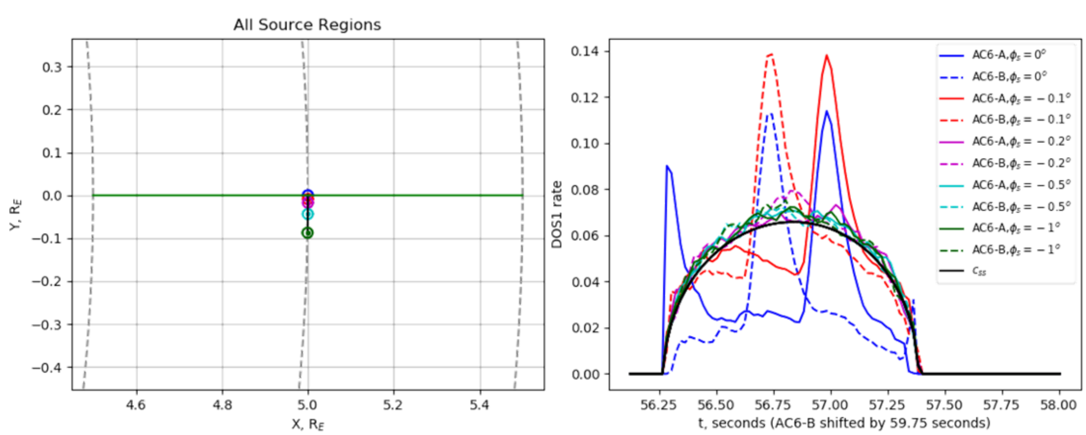

Figure 4. Single sources on a drift shell at $L = 5$. Left: the scene as viewed in the magnetic equator. Sources are small circles, to scale. Gray rings indicate drift shells every 0.5 L. Right: Dosimeter count rates computed at AC6-A and -B for the scene on the left,

with AC6-B shifted by 59.75 seconds. By 0.2° from the center of the source region, the flux has reached steady state. The estimated steady state rate (c_{ss}) is proportional to the path length through the source region, which is given by $\Delta\ell$.

For our next test case, we have sources on three drift shells, $L_s = (4.9,5,5.1)$, and otherwise repeat the setup. Figure 5 shows how such a setup produces persistent curtain-like structures at drift shells conjugate to each of the 3 sources when sources are far away. Microburst-like spikes are superimposed when AC-6 is bounce conjugate to a near source. As before, the time and location of the spikes is different for the two satellites even when AC6-B is shifted in time to line up the satellite locations.

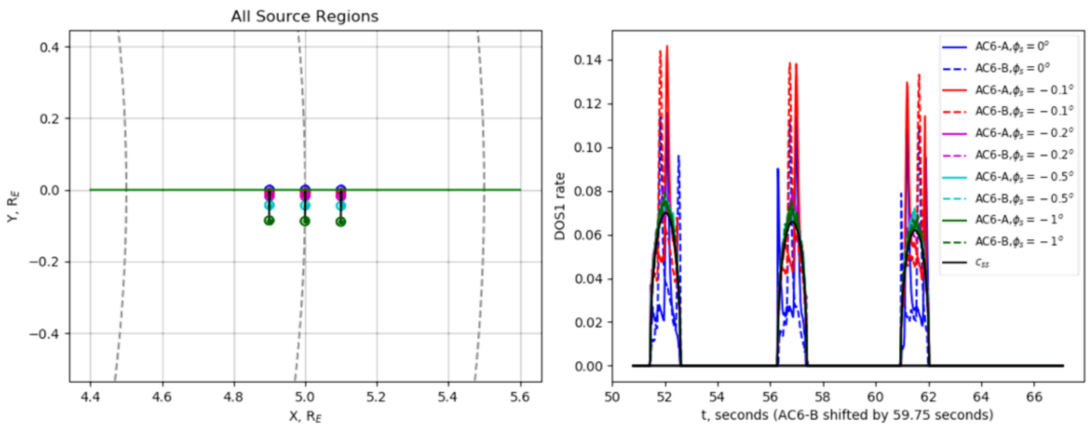

Figure 5. A three-source scene in the format of Figure 5. On the right, the time profile includes microburst-like and curtain-like signatures, depending on the placement of the sources relative to the AC6 trajectory. Far sources produce curtains, near sources produce microbursts.

Next, we look at how the DOS1 rate at AC6 depends on the properties of the source region. We use the same setup as the previous tests, except we have moved the three source region drift shells a bit closer together ($L_s = (4.95,5,5.05)$) to expand the temporal features within each pulse on a narrower time axis. Figure 6 shows studies for the source size (r_s), energy scale (E_s), pulse period (T_s) and pulse width (ΔT_s). Panel (a) shows that the DOS1 response is propotional to r_s in both amplitude and width. The amplitude dependence arises from the longer path length through the circular source region. The width dependence arises from the larger span of drift shells conjugate to AC6. We also note that microburst-like spikes are present farther from the center of the larger source region because even at 0.2°, the $r_s = 150$ km case is still bounce conjugate with the simulated AC6 trajectory.

In panel (b) we show the energy dependence for for the DOS1 rate at AC6. In order to show the curves on the same axis, we have scaled the flux for each source to have the same equatorial DOS1 rate (c_{eq}):

$$c_{\mathrm{eq}} = \int_{E_1}^{E_2} j e^{-E/E_s} R_{\mathrm{DOS1}}(E) dE$$

$$\frac{1}{j_s} = \int_{E_1}^{E_2} e^{-E/E_s} R_{\mathrm{DOS1}}(E) dE$$

This normalization causes the BLC flux (spikes) to be approximately the same order of magnitude for all three spectra. The steady state flux exhibits a residual energy dependence that scales with the ratio of the drift to bounce period, when those periods are evaluated at the 50% level of the weighted energy response shown in Figure 3 and at L_s, and for equatorial pitch angles that mirror at AC6. The dependence on the ratio of periods arises from the fact that the initial microburst packet must spread to fill the bounce path while also spreading in azimuth to fill the gap in the drift phase: the more bounces per drift required, the lower the steady-state flux. Also, there is a hint that the flatter spectrum requires more drift to settle into the steady-state half-circle. This would be consistent with the lower number of bounces per unit drift for higher energy particles. Finally, the spikes at $\varphi_s = 0$ (blue) have the same amplitude across all three sources, accounting for the equatorial flux. That is because the spikes are in the BLC and do not have the phase-mixing ratio dependence that applies only to the steady state rates. The $\varphi_s = 0.1°$ spikes (red) are actually higher because the include significant DLC flux that adds to the BLC flux spikes.

Panel (c) shows that the less frequent the pulse, the lower the DOS1 rate. The steady state DOS1 rates scale inversely proportional to the pulse period T_s, as one would expect for a steady-state condition: the pulse “on” time fraction decreases with $1/T_s$. The third source ($T_s = 5$ s) produces no spikes because the vehicles are not bounce conjugate during any of its pulses.

Panel (d) shows that the peak DOS1 rates scale proportionally with the pulse width ΔT_s. This is also explained by the fact that pulse “on” time is proportional to the pulse width.

Taken together, the steady-state profile at AC6 is given approximately by:

$$c_{\mathrm{SS}} = \frac{\Delta \ell}{2\pi L_s R_E} \frac{\Delta T_s}{T_s} (4\pi \cos \alpha_{lc}) \frac{\tau_d}{\tau_b} c_{eq}$$

The first ratio represents the fraction of the drift orbit covered by the path length through the source. The second ratio is the fraction of time the microburst pulse is on. The factor in parentheses is the solid angle at AC6 in the drift loss cone, where α_{lc} is the loss cone local pitch angle:

$$\sin^2 \alpha_{lc} = \frac{B(L, \theta, \varphi)}{B(L, \frac{\pi}{2} - \lambda_{lc}, \varphi)}$$

The drift to bounce period ratio accounts for how much of a drift is covered by each bounce. Finally, c_{eq} is the DOS1 rate at the center of the equatorial source. This method of estimating c_{SS} is used in Figure 4-Figure 6.

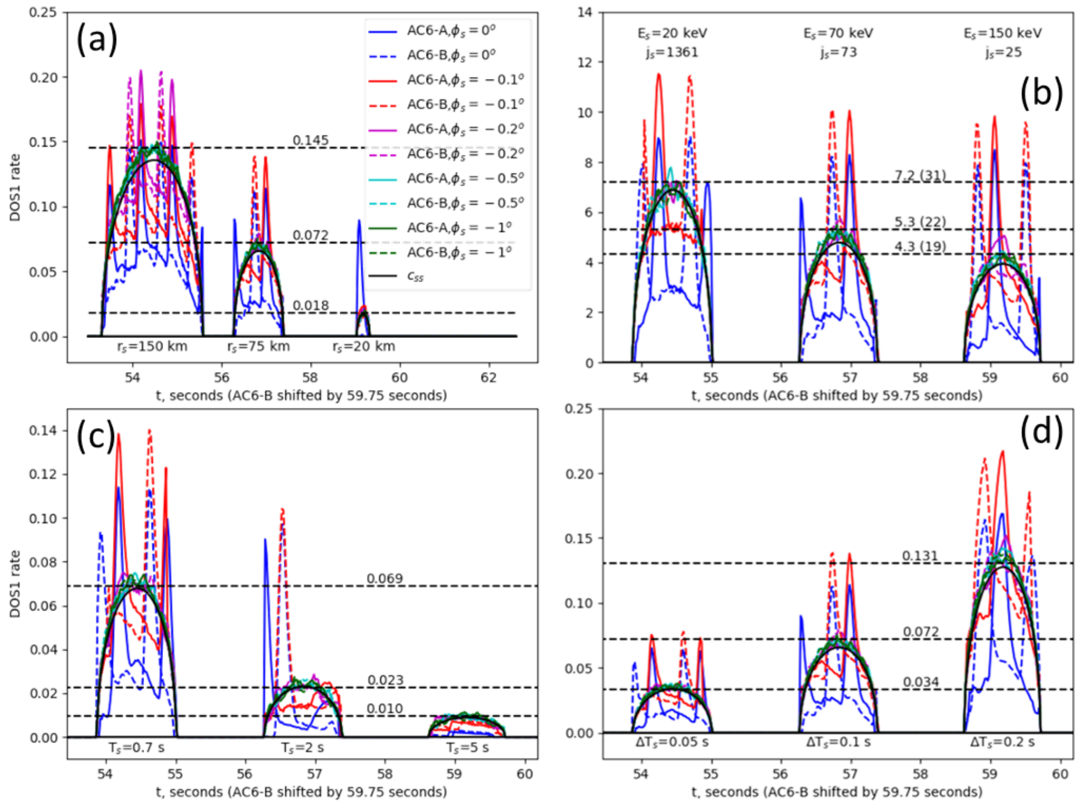

Figure 6. Parameter studies. (a) Comparison of different source region sizes (r_s). (b) Comparison of different source region energy scales (E_s). Note that the source fluxes are normalized so that the equatorial DOS1 rate is constant. The numbers in parentheses are the number of bounces per degree of drift. (c) Comparison of different pulse periods (T_s). (d) Comparison of different pulse widths (ΔT_s). Estimated steady-state rates c_{SS} are provided for each source in black.

4.2 Simulations of a real scene

Next, we consider a real scene observed by AC6. We selected the interval from Figure 2 of *Blake and O'Brien* (2016) because it was confined to a range of L shells somewhat commensurate with the Van Allen Probes data. (The event in Figure 1 extended to $L\sim15$, well outside the observational reach of the probes.) The pass covers the time interval 20:11-20:15 UT on 7 February 2015 for AC6-A, with AC6-B following 65 seconds behind. DOS1 rates observed by both AC6 vehicles are shown Figure 7. In the 1 Hz data shown (which is all that was available for this pass), no microbursts can be observed, but several curtain features are present as most of the temporal structure observed by AC6-A is observed 65 seconds later by AC6-B. AC6-A rates are scaled up by a factor of 4 to match AC6-B. This scaling varies between passes through the radiation belts and is a consequence of AC6-A and -B not actually having identical sensor responses while also sometimes not having the same pitch angle orientation (we neglect the pitch angle response of AC6 throughout this work).

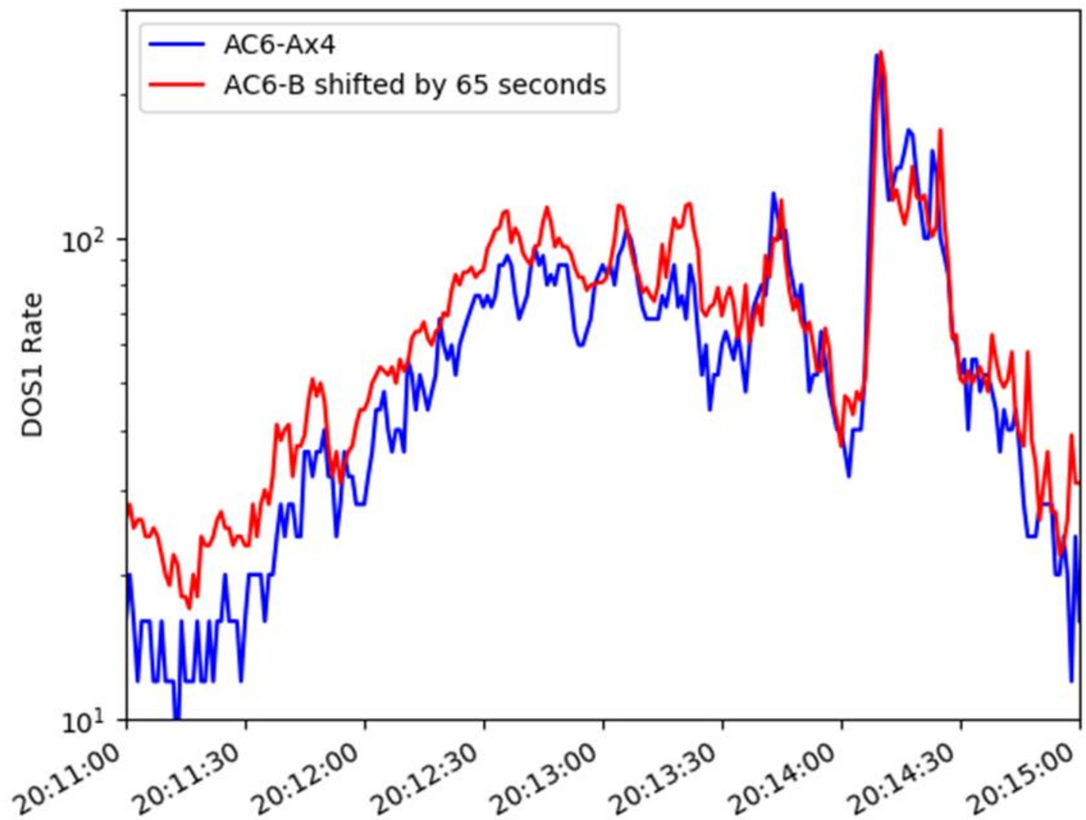

Figure 7. Time profiles observed by AC6. Note the AC6-A DOS1 rate has been scaled up by a factor of 4 to line up with AC6-B. Likewise the AC6-B time profile has been shifted 65 seconds, the in-track lag between the two spacecraft passing the same latitude.

In order to reproduce this scene, first we establish a “background” count rate that represents particles in the drift loss cone from pitch angle scattering at longitudes west of the scene we are constructing. Based on the L profiles of AC-6, we generated the following background as a function of L:

$$c_{\mathrm{bg}} = 60 \times 10^{-\left((L-5.5)/2\right)^2} + 40 \times 10^{-\left((L-8)/2\right)^2}$$

In this formula, we use a dipole L as above. Figure 8 shows the implied DOS1 count rates at RBSP-A and -B as well as the observed AC6-A and -B rates, along with the background rate. In the figure, the abscissa is $L_{m,OPQ}$, which is McIlwain’s L shell parameter in the Olson-Pfitzer Quiet (OPQ) field model (McIlwain, 1961; Olson and Pfitzer, 1977), but the background is evaluated at the dipole L value from the vehicle location, $L = r/\sin^2\theta = r/\cos^2\lambda$. We see that for $L_{m,OPQ} < 5.5$ the equatorial DOS1 count rate would be about ~30 times the rate at AC6-B. However, at higher L, RBSP passes through what is probably a convection boundary and sees a sharp drop in the inferred DOS1 rate followed by spikey rates that are likely a consequence of poor spline fits in the merged flux product. Since RBSP is at local times near midnight, while AC6 is at local times near 0700, the RBSP rates are not necessarily representative of the flux available to be scattered into the DLC and BLC at AC6. As such, the RBSP rates and their underlying fluxes cannot be used as the basis of setting fluxes in the source regions, and the background level at AC6 must be used instead.

We have also indicated in Figure 8 the location of the plasmapause as observed by RBSP EMFISIS. Fine scale structures are observed at AC6 inside the plasmapause at about $L_{m,OPQ}$~4, with no apparent discontinuity in their size or occurrence frequency. Chorus and microbursts are rarely observed inside the plasmapause; nonetheless, for the simulation, we will assume microbursts are present both outside and inside the plasmapause. We will revisit this inconsistency in the discussion and interpretation section below.

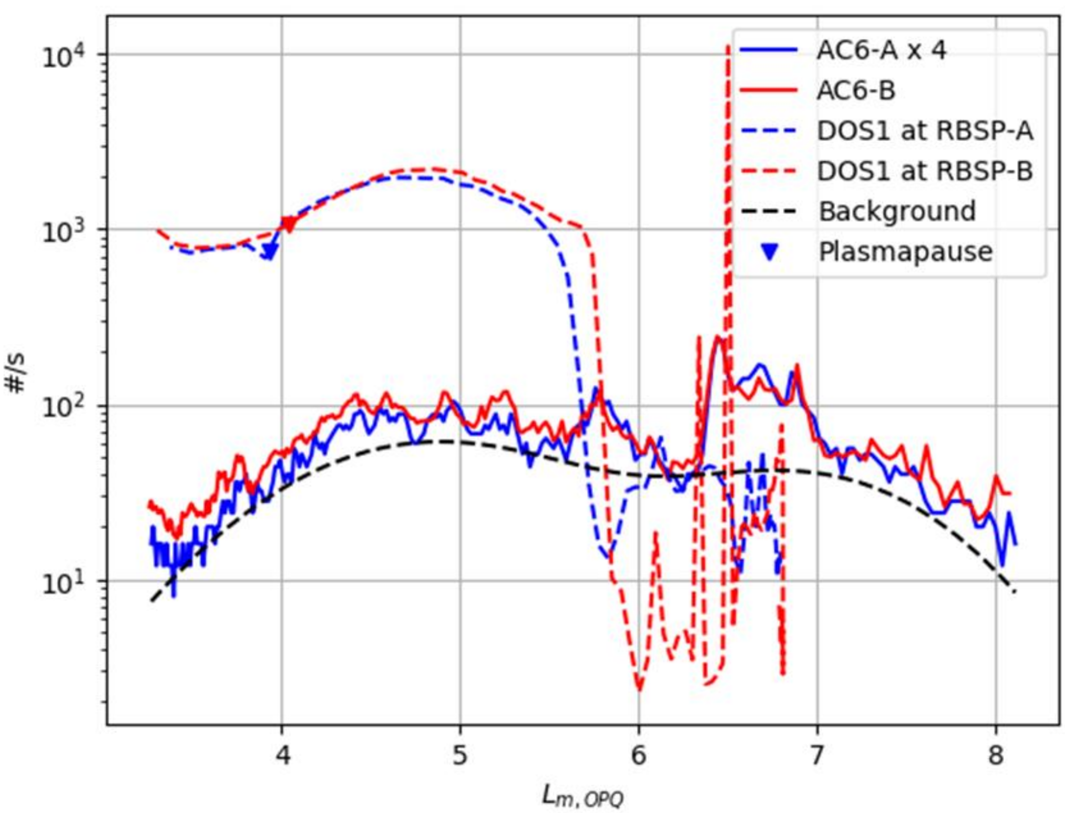

Figure 8. DOS1 count rates observed at AC6 and inferred at RBSP as well as the background rate. Plasmapause crossings by RBSP are indicated as well near $L_{m,OPQ}$~4. Note that the abscissa is McIlwain's L in the OPQ field model.

For this case, where we attempt to simulate a real event, we use Gaussian sources with intensity given by $e^{-\frac{1}{2}(d/r_s)^2}$, where d is the distance from the source's center. The source region is limited to $d < 3r_s$, beyond which the source flux is zero. We use three methods for placing sources in the equatorial plane. All three of these methods have been tuned to reproduce the AC6-A and AC6-B time profiles, scaling either the number of sources or the size of sources to the observed AC6 DOS1 rate.

The first method is the ‘rates’ method in which sources are placed randomly 5-20° west of the AC6-trjaectory. Each source has a radius $r_s = 75$ km, and the number of sources placed is the integer N nearest $N_{\text{goal}} = \frac{c_B}{c_{\text{bg}}} - 1$, where c_B is the DOS1 rate at AC6-B, or 1, whichever is larger. That is, the multiplicity of sources scales with the ratio of the observed AC6-B rate to the background rate. The source flux is $j_s e^{-E/E_s}$, where j_s is:

$$j_{s,\text{rates}} = \frac{1.8 N_{\text{goal}} (L_s/8)^{4.5}}{N \int_{E_1}^{E_2} e^{-E/E_s} R_{\text{DOS1}}(E) dE}$$

The 1.8 and $(L_s/8)^{4.5}$ factors were determined empirically to produce a good match between the rate computed at AC6 and the rate observed by AC6. The integral in the denominator normalizes by the integrated response if there were no losses from the equator to AC6, and the ratio of *N*’s corrects for the round-off errors when placing a discrete number of sources.

The second method for placing sources is the ‘peaks’ method, in which local maxima are found in the ratio of the observed AC6-B DOS1 rate to the background rate. The size of each source is scaled to the size of that ratio: bigger sources should produce higher rates, in proportion to the radius of the source. Starting with the highest peak in the ratio, its L_s is recorded as a source location and then the next peak is found by finding the next highest value in the ratio that is not within 0.05 L of any prior sources. The locations of the sources are shown in Figure 9. Note that sources are generated until the entire time series is covered within 0.05 L of at least one peak, so that some sources are not at local maxima, but merely fill in between others. For each source, the longitude is randomly selected 5-20° west of the AC6-trjaectory, with:

$$r_{s,\text{peaks}} = \frac{100 c_{\text{B}} (8/L_s)}{c_{\text{bg}}}$$

$$j_{s,\text{peaks}} = \frac{0.4 (L_s/8)^{5.5}}{\int_{E_1}^{E_2} e^{-E/E_s} R_{\text{DOS1}}(E) dE}$$

The radius scales with L_s and the ratio of observed DOS1 rate to the background rate. The flux intensity scales only with $(L_s/8)^{5.5}$. As before, these scaling were determined empirically to obtain a good fit to the observed DOS1 rate at AC6-B. We note that the combined L dependence of $r_{s,\text{peaks}} \times j_{s,\text{peaks}}$ is $(L_s/8)^{4.5}$ as with the ‘rates’ method.

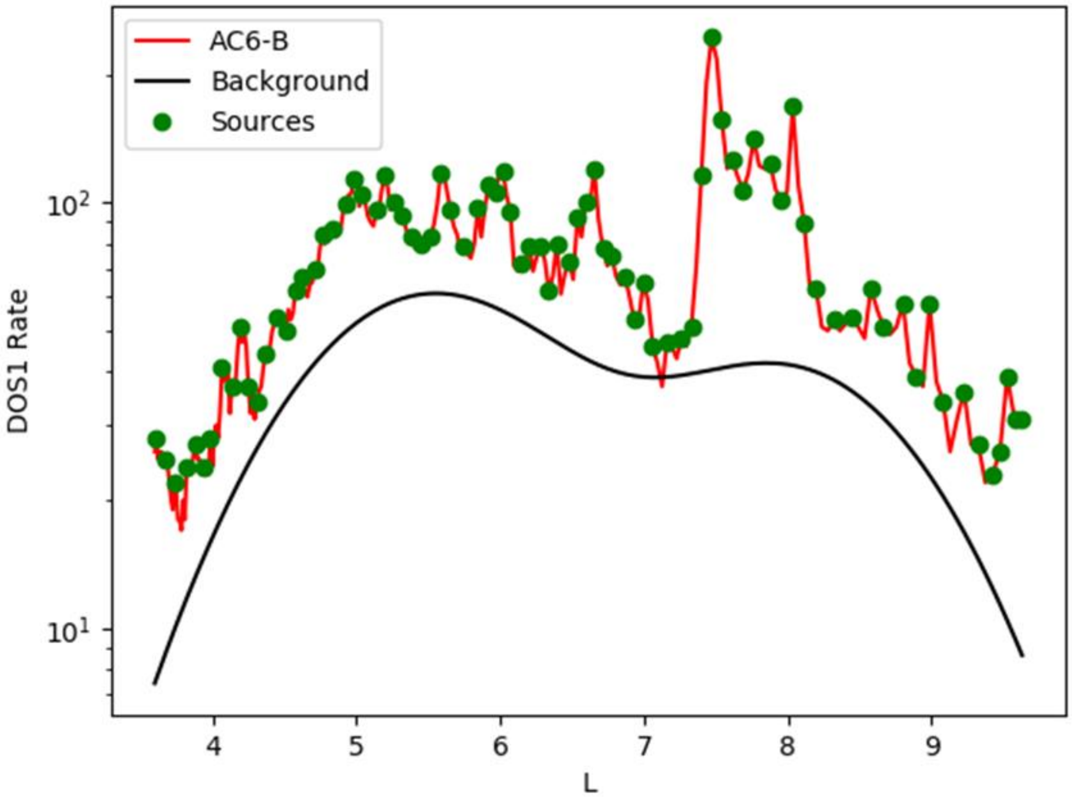

Figure 9. Background and sources identified by the 'peaks' method. The abscissa is dipole *L*.

The final method is the ‘clusters’ method. It follows the ‘peaks’ method, but each large source is replaced by a collection of smaller sources with radii $r_{s,\mathrm{clusters}}$~75 km. The smaller sources are distributed randomly across the original Gaussian source in proportion to the local flux, except that as the sources are created, new sources are randomly rejected if they overlap old sources. Sources at the exact same center are always rejected, with the probability of rejection decreasing linearly to zero as the distance between centers drops to 75 km. Once sources are placed, their radii are scaled so that the total luminosity (flux integrated over area) of the cluster of sources matches that of the corresponding large source from the ‘peaks’ method.

With these three methods in hand for deploying sources in the equatorial plane, we perform the particle tracing simulation using 18 pitch angles (5° spacing) and trace particles backward every 0.1 second, then we compute 1-second averages for comparison to the AC6 observations. Figure 10 shows the setup and results of these simulations. Panel (a) shows many small sources distributed randomly in azimuth but with their concentration in *L* modulated by the observed AC6-B rate. Panel (b) shows that this spatial distribution of sources readily reproduces at both AC6-A and AC6-B the time profile observed at AC6-B. Panel (c) shows the sources for the peaks method, where the smaller number of sources now have their size modulated by the observed AC6-B rate. Panel (d) shows that this distribution of sources can produce curtain-like features. Panel (e) shows the sources from panel (c) broken into clusters of smaller sources. Finally, panel (f) shows that the clusters of sources can also produce curtain-like features. Although the results in (d) and (f) do not fit as well as in (b), that is surely just a matter of fine tuning the method for placing sources. Qualitatively, all three source methods exhibit curtain-like features.

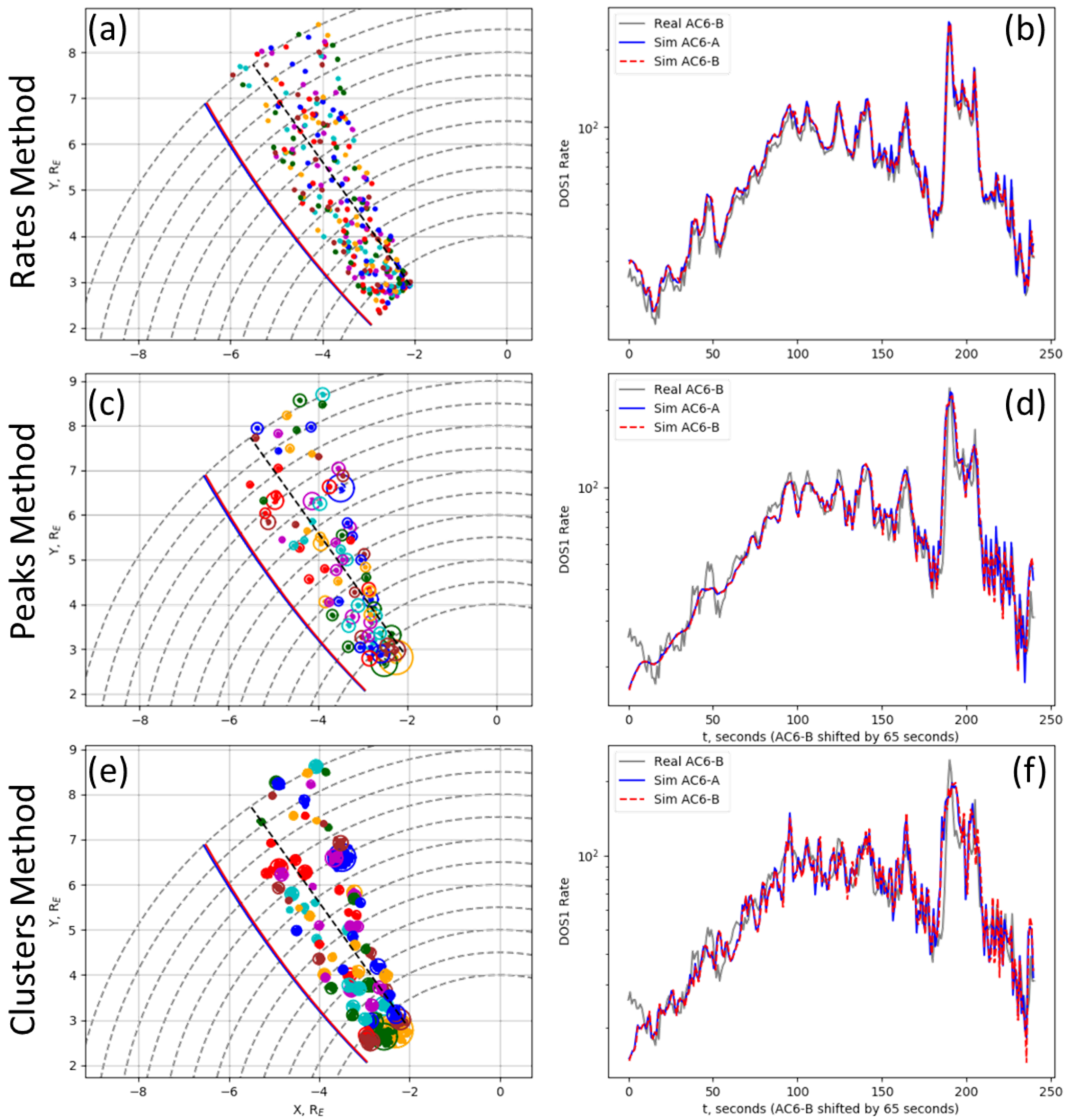

Figure 10. Scenes and resulting AC6-A and AC6-B simulated rates for three source generation methods. Left panels indicate the location of sources, with circles indicating the extent of each Gaussian source, at $3r_s$. In panel (e), larger circles indicate the extent of each cluster. Right panels indicate the observed AC6-B DOS1 rate and the simulated AC6-A and AC6-B rates. DOS1 rates are 1-second averages.

Next, we confirm that these source patterns also produce microbursts. For these simulations, we sample at 50 Hz and compute 0.1 second averages, which is representative of the AC6 high-rate data that has been shown to detect microbursts (e.g., *Shumko et al.*, 2020b). Figure 11 shows the results for the three source methods shown in Figure 10 for a vehicle that flies along the black trajectory through the source region. We again simulated AC6-B being 65 seconds behind AC6-A. The left panels show the entire interval – there are fewer curtains because many sources are to the east of the trajectory. The right panel zooms in on one curtain whose source region is particularly close to the simulated trajectory. Each case shows that there are several microburst pulses superimposed on the curtain profile. While the curtain profile is in very good agreement between AC6-A and AC6-B along this simulated trajectory, the spikes are offset in time between AC6-A and AC6-B indicating they are temporal features, like microbursts. The spikes are produced by bounce-loss-cone fluxes that are present only when the source is pulsed on. With both the realistic scene and this microburst reconstruction in hand, we can turn to interpretation of these collected results.

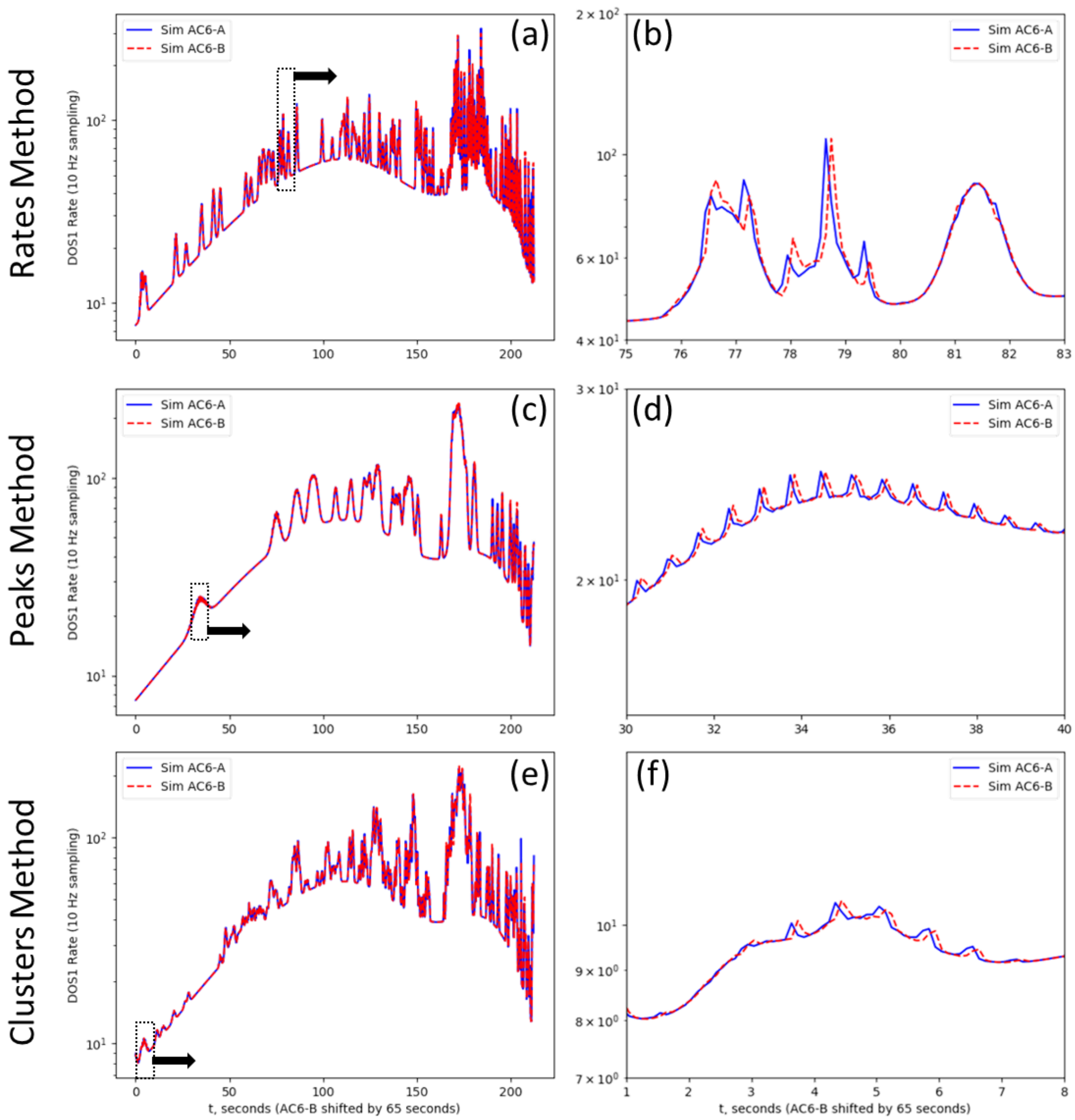

Figure 11. AC6 DOS1 rates simulated for a crossing through the source regions shown in Figure 10 (black trajectories therein). One row for each source placement method. Each right panel zooms in on a small region of its time profile, where pulsing microburst-like signatures are seen superimposed on the broad curtain-like feature. DOS1 rates are 0.1-second averages.

5 Discussion and Interpretation

Our simulations show clearly that it is possible to produce curtains from pulsing microbursts. There are multiple configurations of microburst source regions, with varying distribution in size and azimuth, that can produce a given time profile of curtains at AC6. Within the time profiles produced by these sources, there are microburst-like temporal features observed on a simulated trajectory through the source region. On account of the degeneracy in source distribution, it is likely that pulsing sources could be replaced by non-periodic or even single-pulse source regions and still produce the profile observed at AC6. All that appears to be required is a radially structured distribution of microburst sources a few degrees west of the AC6 trajectory.

Of primary importance is the radial structure of the microburst source distribution, which is likely a reflection of the equatorial distribution of chorus waves (e.g., *Breneman et al.* 2017). The 'rates' and 'clusters' source methods are consistent with the results of *Shumko et al.* (2020b), who found that inferred microburst sizes in the equatorial plane were often less than 100 km. The difference between these methods is that in the 'rates' method, there is no azimuthal clustering of the sources. Specifically, the 'clusters' ties the microbursts together into spatially distinct regions such as reported by *Shumko et al.* (2017) and *Anderson et al.* (2017). The 'peaks' method source sizes are mainly distributed from r_S~130 to 450 km with a ~5% tail that extends out to 800 km. That distribution is consistent with larger (~500 km) sources reported by *Crew et al.* (2016) and *Shumko et al.* (2018). Coherently pulsing aurora map to even larger equatorial scale sizes, up to ~5000 km (e.g., *Nishimura et al.*, 2010;2011). The variety of scale sizes present in the literature can partially be resolved by recognizing that there are different definitions of microburst size based on phase coherence, amplitude coherence, or general simultaneity, with these three different phenomenological sizes progressing from smallest to largest in physical extent. In our 'rates' and 'peaks' simulations the microbursts are amplitude and phase coherent. In our 'clusters' simulations, the cluster itself can be thought of as an amplitude coherent region, whereas the individual constituent sources represent phase-coherent sub-regions. The underlying chorus waves have a somewhat different set of scale sizes, what *Agapitov et al.* (2011; 2017; 2018 2021) call spatial extent (1000s km), amplitude distribution (100s km), and coherence extent (< 100 km). It should be noted that the phase involved in phase coherence is the wave phase for a kHz wave, whereas for microburst, the phase is roughly the particle bounce phase – particle sensors typically cannot resolve kHz structure.

What our simulations do not show is dominant microburst structure over a large *L* range, even though this has been reported in many studies (e.g., *Blake et al.*, 1996; *Nakamura et al.*, 2000; *Lorentzen et al.*, 2001b; *Blum et al.*, 2015, *Anderson et al.*, 2017). This discrepancy can partially be explained by noting that several of these studies used sensors with different energy response than AC6. Nonetheless, it is likely that there are many more sources in the equatorial plane than we have depicted. Additional non-pulsing sources would easily increase the chance of encountering a microburst without substantially modifying the results of our study. Likewise, replacing each pulsing source with multiple non-pulsing sources on the same azimuth will still produce curtains, although it might not increase the chance of observing microbursts.

Although our simulation included pulsing microbursts that continue indefinitely, real microburst only pulse for a few to tens of seconds (see, e.g., *Brown et al.*, 1965; *Anderson et al.*, 2017; *Kawamura et al.* 2021, and references therein). However, presumably as one pulsing source region ceases, others may appear nearby if the nearby plasma conditions remain conducive to chorus production.

Another concern with our simulation is the fact that the fine spatial structures appear to extend into the plasmasphere, where chorus is rare. Perhaps these structures are caused by hiss emissions, with the amplitude exhibiting small scales or simply the plasmapsheric density variations modulating the wave-particle resonance. Both hiss and plasma exhibit the small scales (*Agapitov et al.*, 2018; 2021; *Hosseini et al.* 2021), but hiss does not produce microbursts. So, at a minimum, explaining fine structure inside the plasmasphere would require a reformulation of the source region, not to pulse, but to be a steady, but spatially-structure, scattering source. To produce identifiable curtains, such a source would need to be either more intense or more extended in longitude than its neighbors to avoid being lost in the confusion of other sources. Explaining curtains in the plasmasphere will be an interesting topic for future work.

6 Conclusions

We have verified through numerical simulation that pulsing microburst sources in the equatorial plane can produce stable fine structure in precipitation observed at low altitudes. We have been able to verify that microbursts can add up to curtains as hypothesized by *Blake and O'Brien* (2016), through accumulated flux in the drift loss cone. However, we have also learned that AC6 data, at least as we have analyzed it, does not provide strong constraints on microburst source distributions. The curtains are a projection of the drift-integrated radial distribution of microburst luminosity, but they do not discriminate among a variety of possible source distributions. Also, given that some curtains are observed inside the plasmapause, it seems likely that a hiss-related mechanism could be necessary. Additionally, if AC6 sampling bias did not confound the results, *Shumko et al.* (2020a) showed a local time distribution of curtains not wholly consistent with a chorus source. Finally, as *Shumko et al.* (2020a) showed curtains in the bounce loss cone, the microburst origin hypothesis cannot be the sole explanation for curtains. Additional research will be required to determine if additional hypotheses are required or simply more apt than the microburst hypothesis.

Acknowledgments: The authors thank many colleagues for help conducting this study: J. Blake for extensive inspection of AC6 data and events and discussions of curtain and microburst phenomenology, B. Kwan and A. Halford for initial investigations of test particle tracing and description of microbursts sources, M. Shumko and A. Agapitov for extensive discussions about microbursts and curtains scale sizes and phenomenology and A. Boyd for assistance with the Van Allen Probes data. This project was funded by NASA HUSPI contract 80NSSC18K0309. AeroCube-6 data are hosted at cdaweb.gsfc.nasa.gov, but the comma separated values files used in this study can be found at rbspgway.jhuapl.edu/ac6 or spdf.gsfc.nasa.gov/pub/data/-aaa_smallsats_cubesats/aerocube/aerocube-6. Processing and analysis of the Van Allen Probes data was supported by Energetic Particle, Composition, and Thermal Plasma

(RBSP-ECT) investigation funded under NASA's Prime contract no. NAS5-01072. All RBSP-ECT data are publicly available at the Web site rbsp-ect.newmexicoconsortium.org. Plasmapause locations are available from the EMFISIS science operations center emfisis.physics.uiowa.edu. Magnetic index data (Kp, Dst) can be obtained from omniweb.gsfc.nasa.gov. The cited Aerospace Technical Reports, AeroCube-6 sensor response and time series data, the Van Allen Probes data, used in this study can be found at doi:10.5281/zenodo.5796339, and the source code can be found at github.com/tpoiii/dipole_tracer_ac6 or at doi:10.5281/zenodo.6011631.

7 References

Agapitov, O., Blum, L. W., Mozer, F. S., Bonnell, J. W., & Wygant, J. (2017). Chorus whistler wave source scales as determined from multipoint Van Allen Probe measurements. *Geophysical Research Letters, 44*, 2634-2642. https://doi.org/10.1002/2017GL072701

Agapitov, O., Krasnoselskikh, V., Dudok de Wit, T., Khotyaintsev, Y., Pickett, J. S., Santolik, O., & Rolland, G. (2011). Multispacecraft observations of chorus emissions as a tool for the plasma density fluctuations' remote sensing. *Journal of Geophysical Research, 116*, A09222. https://doi.org/10.1029/2011JA016540

Agapitov, O., Mourenas, D., Artemyev, A., Breneman, A., Bonnell, J. W., Hospodarsky, G., & Wygant, J. (2021). Chorus and hiss scales in the inner magnetosphere: Statistics from high-resolution filter bank (FBK) Van Allen proves multi-point measurements. *Journal of Geophysical Research: Space Physics, 126*, e2020JA028998. https://doi.org/10.1029/2020JA028998

Agapitov, O. V., Mourenas, D., Artemyev, A. V., Mozer, F. S., Bonnell, J. W., Angelopoulos, V., et al. (2018). Spatial extent and temporal correlation of chorus and hiss: Statistical results from multipoint THEMIS observations. *Journal of Geophysical Research-A: Space Physics, 123*(10), 8317–8330. https://doi.org/10.1029/2018JA025725

Anderson, B., Shekhar, S., Millan, R., Crew, A., Spence, H., Klumpar, D., Blake, J. B., O'Brien, T. P., & Turner, D. (2017). Spatial scale and duration of one microburst region on 13 August 2015. Journal of Geophysical Research: Space Physics, 122, 5949–5964. https://doi.org/10.1002/2016JA023752

Blake, J. B., Looper, M. D., Baker, D. N., Nakamura, R., Klecker, B., & Hovestadt, D. (1996). New high temporal and spatial resolution measurements by SAMPEX of the precipitation of relativistic electrons. Advances in Space Research, 18(8), 171–186. https://doi.org/10.1016/0273-1177(95)00969-8

Blake, J. B., & O'Brien, T. P. (2016). Observations of small-scale latitudinal structure in energetic electron precipitation. Journal of Geophysical Research: Space Physics, 121, 3031–3035. https://doi.org/10.1002/2015JA021815

Blum, L., Li, X., & Denton, M. (2015). Rapid MeV electron precipitation as observed by SAMPEX/HILT during high-speed stream-driven storms. Journal of Geophysical Research: Space Physics, 120, 3783–3794. https://doi.org/10.1002/2014JA020633

Boyd, A. J., Reeves, G. D., Spence, H. E., Funsten, H. O., Larsen, B. A., Skoug, R. M., et al. (2019). RBSP-ECT combined spin-averaged electron flux data product. *Journal of Geophysical Research: Space Physics, 124*, 9124-9136. https://doi.org/10.1029/2019JA026733

Breneman, A., Crew, A., Sample, J., Klumpar, D., Johnson, A., Agapitov, O., Shumko, M., Turner, D. L., Santolik, O., Wygant, J. R., Cattell, C. A., Thaller, S., Blake, B., Spence, H., & Kletzing, C. A. (2017). Observations directly linking relativistic electron microbursts to whistler mode chorus: Van Allen Probes and FIREBIRD II. Geophysical Research Letters, 44, 11,265–11,272. https://doi.org/10.1002/2017GL075001

Brown, R., Barcus, J., & Parsons, N. (1965). Balloon observations of auroral zone X rays in conjugate regions. 2. Microbursts and pulsations. Journal of Geophysical Research, 70, 2599–2612. https://doi.org/10.1029/JZ070i011p02599

Crew, A. B., Spence, H. E., Blake, J. B., Klumpar, D. M., Larsen, B. A., O'Brien, T. P., Driscoll, S., Handley, M., Legere, J., Longworth, S., Mashburn, K., Mosleh, E., Ryhajlo, N., Smith, S., Springer, L., & Widholm, M. (2016). First multipoint in situ observations of electron microbursts: Initial results from the NSF FIREBIRD II mission. Journal of Geophysical Research: Space Physics, 121, 5272–5283. https://doi.org/10.1002/2016JA022485

Hosseini, P., Agapitov, O., Harid, V., & Gołkowski, M. (2021). Evidence of small scale plasma irregularity effects on whistler mode chorus propagation. *Geophysical Research Letters, 48*, e2021GL092850. https://doi.org/10.1029/2021GL092850

Johnson, A. T., Shumko, M., Sample, J., Griffith, B., Klumpar, D., Spence, H., & Blake, J. B. (2021). The energy spectra of electron microbursts between 200 keV and 1 MeV. *Journal of Geophysical Research: Space Physics*, *126*, e2021JA029709. https://doi.org/10.1029/2021JA029709

Kawamura, M., Sakanoi, T., Fukizawa, M., Miyoshi, Y., Hosokawa, K., Tsuchiya, F., et al. (2021). Simultaneous pulsating aurora and microburst observations with ground-based fast auroral imagers and CubeSat FIREBIRD-II. *Geophysical Research Letters, 48*, e2021GL094494. https://doi.org/10.1029/2021GL094494

Kletzing, C. A., Kurth, W. S., Acuna, M., MacDowall, R. J., Torbert, R. B., Averkamp, T.,…Tyler, J. (2013). The Electric and Magnetic Field Instrument Suite and Integrated Science (EMFISIS) on RBSP. *Space Science Reviews, 179*, 127–181. https://doi.org/10.1007/s11214-013-9993-6

Lee, J.-J., et al. (2005), Energy spectra of ∼170–360 keV electron microbursts measured by the Korean STSAT-1, *Geophys. Res. Lett., 32*, L13106, doi:10.1029/2005GL022996.

Lorentzen, K. R., J. B. Blake, U. S. Inan, and J. Bortnik, Observations of relativistic electron microbursts in association with VLF chorus, *J. Geophys. Res., 106*, 6017, 2001a.

Lorentzen, K. R., M. D. Looper, and J. B. Blake, Relativistic electron microbursts during the GEM storms, Geophys. Res. Lett., 28, 2573, 2001b.

McIlwain, C. E., Coordinates for Mapping the Distribution of Magnetically Trapped Particles, *J. Geophys. Res., 66*, pp. 3681-3691, 1961.

Nakamura, R., Isowa, M., Kamide, Y., Baker, D. N., Blake, J. B., and Looper, M. (2000), SAMPEX observations of precipitation bursts in the outer radiation belt, *J. Geophys. Res., 105*(A7), 15875– 15885, doi:10.1029/2000JA900018.

Nishimura, Y., et al. (2010), Identifying the driver of pulsating aurora, *Science, 330*, 81, doi:10.1126/science.1193186.

Nishimura, Y., et al. (2011), Multievent study of the correlation between pulsating aurora and whistler mode chorus emissions, *J. Geophys. Res.*, *116*, A11221, doi:10.1029/2011JA016876.

Northrop, T.G. and E. Teller (1960) Stability of adiabatic motion of charged particles in the Earth's field, *Phys. Rev.*, *117*(1), 215-225.

O'Brien, T. P., Blake, J. B., & Gangestad, J. W. (2016). AeroCube-6 dosimeter data README (Tech. Rep. No. TOR-2016-01155). The Aerospace Corporation.

O'Brien, T. P., Looper, M. D., & Blake, J. B. (2019). AeroCube-6 dosimeter equivalent energy thresholds and flux conversion factors (Tech. Rep. No. TOR-2017-02598). The Aerospace Corporation.

Olson, W. P., and K. A. Pfitzer (1977), Magnetospheric magnetic field modeling, Annual Scientific Report, Air Force Office of Scientific Research contract F44620-75-C-0033, McDonnell Douglas Astronautics Co., Huntington Beach, Calif.

Santolík, O., D. A. Gurnett, and J. S. Pickett (2004), Multipoint investigation of the source region of storm-time chorus, *Ann. Geophys.*, *22*, 2555– 2563, doi:10.5194/angeo-22-2555-2004.

Schulz, M., and L. J. Lanzerotti (1974), Physics and Chemistry in Space, Particle Diffusion in the Radiation Belts, vol. 7, Springer, New York.

Shue, J.-H., Hsieh, Y.-K., Tam, S. W. Y., Wang, K., Fu, H. S., Bortnik, J., Tao, X., Hsieh, W.-C., and Pi, G. (2015), Local time distributions of repetition periods for rising tone lower band chorus waves in the magnetosphere, *Geophys. Res. Lett.*, *42*, 8294– 8301, doi:10.1002/2015GL066107.

Shumko, M., Johnson, A. T., O'Brien, T. P., Turner, D. L., Greeley, A. D., Sample, J. G., et al. (2020a). Statistical properties of electron curtain precipitation estimated with AeroCube-6. *Journal of Geophysical Research: Space Physics*, *125*, e2020JA028462. https://doi.org/10.1029/2020JA028462

Shumko, M., Johnson, A., Sample, J., Griffith, B. A., Turner, D. L., O'Brien, T. P., Agapitov, O., Blake, J. B., & Claudepierre, S. G. (2020b). Electron microburst size distribution derived with AeroCube-6. Journal of Geophysical Research: Space Physics, 125, e2019JA027651. https://doi.org/10.1029/2019JA027651

Walt, M. (1994), Introduction to Geomagnetically Trapped Radiation, Cambridge U P, Cambridge.